The Astrophysical Journal, 693:1209–1218, 2009 March 10 doi:10.1088/0004-637X/693/2/1209

PHOTODESORPTION OF ICES. II. H_2O AND D_2O

Karin I. Öberg[1], Harold Linnartz[1], Ruud Visser[2], and Ewine F. van Dishoeck[2,3]
[1] Raymond and Beverly Sackler Laboratory for Astrophysics, Leiden Observatory, Leiden University, P.O. Box 9513, NL 2300 RA Leiden, The Netherlands; oberg@strw.leidenuniv.nl
[2] Leiden Observatory, Leiden University, P.O. Box 9513, NL 2300 RA Leiden, The Netherlands
Received 2008 September 9; accepted 2008 December 11; published 2009 March 5

ABSTRACT

Gaseous H_2O has been detected in several cold astrophysical environments, where the observed abundances cannot be explained by thermal desorption of H_2O ice or by H_2O gas-phase formation. These observations hence suggest an efficient nonthermal ice desorption mechanism. Here, we present experimentally determined UV photodesorption yields of H_2O and D_2O ices and deduce their photodesorption mechanism. The ice photodesorption is studied under ultrahigh vacuum conditions and at astrochemically relevant temperatures (18–100 K) using a hydrogen discharge lamp (7–10.5 eV), which simulates the interstellar UV field. The ice desorption during irradiation is monitored using reflection absorption infrared spectroscopy of the ice and simultaneous mass spectrometry of the desorbed species. The photodesorption yield per incident photon, $Y_{pd}(T, x)$, is identical for H_2O and D_2O and its dependence on ice thickness and temperature is described empirically by $Y_{pd}(T, x) = Y_{pd}(T, x > 8)(1 - e^{-x/l(T)})$, where x is the ice thickness in monolayers (MLs) and $l(T)$ is a temperature-dependent ice diffusion parameter that varies between ∼1.3 ML at 30 K and 3.0 ML at 100 K. For thick ices, the yield is linearly dependent on temperature due to increased diffusion of ice species such that $Y_{pd}(T, x > 8) = 10^{-3}\,(1.3 + 0.032 \times T)$ UV photon^{-1}, with a 60% uncertainty for the absolute yield. The increased diffusion also results in an increasing H_2O:OH desorption product ratio with temperature from 0.7:1.0 at 20 K to 2.0:1.2 at 100 K. The yield does not depend on the substrate, the UV photon flux, or the UV fluence. The yield is also independent of the initial ice structure since UV photons efficiently amorphize H_2O ice. The results are consistent with theoretical predictions of H_2O photodesorption at low temperatures and partly in agreement with a previous experimental study. Applying the experimentally determined yield to a Herbig Ae/Be star+disk model provides an estimate of the amount of gas-phase H_2O that may be observed by, e.g., *Herschel* in an example astrophysical environment. The model shows that UV photodesorption of ices increases the H_2O content by orders of magnitude in the disk surface region compared to models where nonthermal desorption is ignored.

Key words: astrochemistry – circumstellar matter – ISM: molecules – methods: laboratory – molecular data – molecular processes – ultraviolet: ISM

1. INTRODUCTION

H_2O, in solid or gaseous form, is one of the most common species in molecular clouds, typically only second to H_2 and sometimes to CO. This makes H_2O, together with CO, the dominant reservoir of oxygen during the critical stages of star formation (van Dishoeck et al. 1993). H_2O is thus a key molecule in astrochemical models and its partitioning between the grain and gas phase therefore has a large impact on the possible chemical pathways, including the formation of complex organics (Charnley et al. 1992; van Dishoeck 2006).

In cold, quiescent clouds H_2O forms through hydrogenation of O (O_2 or O_3) on cold (sub)micron-sized silicate grain surfaces forming icy layers (Tielens & Hagen 1982; Léger et al. 1985; Boogert & Ehrenfreund 2004; Miyauchi et al. 2008; Ioppolo et al. 2008). Other ices, like NH_3 and CH_4, probably form similarly, but observations show that H_2O is the main ice constituent in most lines of sight (LOS), with a typical abundance of 1×10^{-4} with respect to the number density of hydrogen nuclei. Gas-phase H_2O formation is only efficient above 300 K (Elitzur & Watson 1978; Elitzur & de Jong 1978; Charnley 1997). At lower temperatures gas-phase ion–molecule reactions maintain a low H_2O abundance around 10^{-7} (Bergin et al. 1995). Any higher abundances require either thermal desorption of the H_2O ice above ∼100 K or nonthermal desorption at lower temperatures (Bergin et al. 1995; Fraser et al. 2001).

Gas-phase H_2O is observed from the ground only with great difficulty. Still both isotopic and normal H_2O have been detected in astrophysical environments from ground-based telescopes (Jacq et al. 1988; Knacke & Larson 1991; Cernicharo et al. 1990; Gensheimer et al. 1996; van der Tak et al. 2006). The *Infrared Space Observatory* (*ISO*) detected warm H_2O gas unambiguously toward several low- and high-mass young stellar objects (van Dishoeck & Helmich 1996; Ceccarelli et al. 1999; Nisini et al. 1999; Boonman & van Dishoeck 2003). *ISO* was followed by two other space-based telescopes, the *Submillimeter Wave Astronomy Satellite* (*SWAS*) and *Odin*. In difference to *ISO*, *SWAS*, and *Odin* are capable of detecting the fundamental ortho-H_2O 1_{10}–1_{01} transition at 538.3 μm and hence probe cold H_2O gas (Melnick et al. 2000; Hjalmarson et al. 2003). Both telescopes have observed H_2O gas toward star-forming regions and detected the expected enhancements near protostars and in outflows where thermal ice desorption or gas-phase formation is possible (Hjalmarson et al. 2003; Franklin et al. 2008). Critical for the present study, H_2O gas has also been detected toward photon-dominated regions (Snell et al. 2000; Wilson et al. 2003) and is also more abundant toward diffuse than toward dense clouds. These two results point to an efficient ice photodesorption mechanism (Melnick & Bergin 2005). The importance of photodesorption at the edges of clouds has more recently been modeled by Hollenbach

[3] Also at Max-Planck Institut für Extraterrestrische Physik (MPE), Giessenbachstraat 1, D 85748 Garching, Germany.

et al. (2009). They find that the H_2O gas abundance is enhanced by orders of magnitude at $A_V = 2$–8 mag into the cloud when including photodesorption of H_2O ice in their model at a rate derived from the results by Westley et al. (1995a). Circumstellar disks is a second region where the impact of photodesorption is expected to be large. Willacy & Langer (2000) showed that a photodesorption yield of 10^{-3} molecules photon^{-1} is enough to explain the observed gas-phase CO abundances in the outer regions of flared disks. Employing a similar photodesorption yield for H_2O ice, the disk models of Dominik et al. (2005) and Willacy (2007) both predict the existence of significant amounts of gas-phase H_2O in a layer above the midplane region.

With the advent of the *Herschel Space Observatory*, cold and warm H_2O gas observations on scales of protostellar envelopes and disks will for the first time become possible (van Kempen et al. 2008). In preparation for these and other observations, and to interpret data from *Odin* and *SWAS*, nonthermal processes need to be better understood. These nonthermal desorption processes include ion/electron sputtering, desorption due to the release of chemical energy, and photodesorption. Of these, sputtering of ice by electrons and ions, has been investigated over a range of conditions during the past few decades (e.g., Brown et al. 1978; Famá et al. 2008) and the dependences of the yield on, e.g., ice temperature, projectile type, and energy are rather well understood. In contrast, only a handful of laboratory studies exists on the efficiency of ice photodesorption (e.g., Westley et al. 1995a; Öberg et al. 2007b, 2009).

Westley et al. (1995a, b) determined the photodesorption rate of H_2O ice experimentally to be $3–8\times10^{-3}$ molecules per UV photon for a 500 nm thick H_2O ice. In their experiment the photodesorption rate depends on UV fluence as well as temperature. The photon fluence dependence, together with the observed gas-phase H_2 and O_2 during irradiation, was taken as evidence that H_2O photodesorption at low temperatures mainly occurs through desorption of photoproducts rather than of H_2O itself. Several questions remain regarding the applicability of their study to astrophysical regions due to the uncertainty of the proposed mechanism. In addition, their dependence on photon fluence is not reproduced in recent CO and CO_2 photodesorption experiments and cannot easily be explained theoretically (Andersson et al. 2006; Öberg et al. 2007b, 2009; Andersson & van Dishoeck 2008).

In a different experiment, Yabushita et al. (2006) investigated H-atom photodesorption from H_2O ice during irradiation at 157 and 193 nm using time-of-flight mass spectrometry. They found that the temperature and hence the origin of the desorbed H atoms varies significantly between crystalline and amorphous ices at 100 K. This indicates that photodesorption depends on the ice morphology, which is in contrast to the findings of Westley et al. (1995a). Desorption of recombined D_2 during irradiation of D_2O ice at 12 K has also been found by (Watanabe et al. 2000). Both experiments provide valuable input for models, but cannot directly be used to determine the total H_2O photodesorption rate.

UV irradiation of H_2O ice results in photochemistry products as well as photodesorption. A variety of photochemistry products are readily produced during irradiation of H_2O-dominated ice mixtures (d'Hendecourt et al. 1982; Allamandola et al. 1988). Pure H_2O ice photolysis results in the production of H_2O_2, OH radicals, and HO_2 at 10 K (Gerakines et al. 1996; Westley et al. 1995b). After a fluence of $\sim5 \times 10^{18}$ UV photons cm^{-2} Gerakines et al. (1996) found that the final band area of the formed H_2O_2 was only ~0.25% compared to the H_2O band area and the OH band area was even smaller. No study exists for higher temperatures, but as photodissociation fragments become more mobile, e.g., O_2 formation would be expected (Westley et al. 1995a).

Only a handful models of ice photodesorption exists in the literature. Andersson et al. (2006) and Andersson & van Dishoeck (2008) have investigated H_2O photochemistry and photodesorption theoretically using classical dynamics calculations. In the simulations they followed H_2O dissociation fragments, after the absorption of a UV photon, in the top six monolayers (MLs) of both crystalline and amorphous H_2O ices at 10 K. For each ice they found that desorption of H_2O has a low probability (less than 0.5% yield per absorbed UV photon) for both types of ices. The total H_2O photodesorption yield from the top six ice layers was calculated to be $\sim4 \times 10^{-4}$ molecules per incident UV photon.

In the present study, we aim at determining experimentally the photodesorption yields of H_2O and D_2O and their dependences on ice thickness, temperature, morphology, UV flux, and fluence as well as irradiation time. We use these results as input for an astrophysical model of a typical circumstellar disk to estimate the impact of photodesorption and to predict the observable column densities of H_2O as relevant to, e.g., upcoming *Herschel* programs.

2. EXPERIMENTS AND DATA ANALYSIS

2.1. Experiments

The experimental setup (CRYOPAD) is described in detail by Fuchs et al. (2006) and Öberg et al. (2007b). The setup allows simultaneous detection of molecules in the gas phase by quadrupole mass spectrometry (QMS) and in the ice by reflection absorption infrared spectroscopy (RAIRS) using a Fourier transform infrared (FTIR) spectrometer. The FTIR covers 1200–4000 cm^{-1} with a typical spectral resolution of 1 cm^{-1}. The experimental procedure to derive photodesorption yields is described extensively in Öberg et al. (2009), where the photodesorption measurements of CO, N_2, and CO_2 ices are reported. Here, the procedure is summarized and only modifications to the procedure are described in detail.

In the experiments, H_2O and D_2O ices of 1.5–28 MLs are grown under ultrahigh vacuum conditions (UHV; $P \sim 10^{-9}$ mbar with the background pressure dominated by H_2) at 18–100 K on a gold substrate that is mounted on the coldfinger of a He cryostat. The H_2O sample is prepared from deionized H_2O that is purified through at least three freeze–thaw cycles. The D_2O sample is measured to have a 90% isotopic purity and is similarly freeze-thawed before use.

Within the experimental uncertainties, we find that there is no difference in the photodesorption rate of 9.5 ML D_2O ice deposited on top of 48 ML H_2O ice compared with 8.9 ML D_2O ice deposited directly onto the gold substrate. Since the nature of the substrate has no influence on the photodesorption, all other experiments are carried out with H_2O or D_2O ice deposited directly on the gold substrate.

The ice films are irradiated at normal or 45° incidence with UV light from a broadband hydrogen microwave discharge lamp, which peaks around Lyα at 121 nm and covers 115–170 nm or 7–10.5 eV (Muñoz Caro & Schutte 2003). The lamp UV photon flux is varied between 1.1×10^{13} and 5.0×10^{13} photons cm^{-2} s^{-1} in the different experiments. The lamp flux is measured by a National Institute of Standards and

Table 1
Summary of H_2O and D_2O Experiments

Experiment	Composition	Temperature (K)	Thickness (ML)	UV Flux (10^{13} cm^{-2} s^{-1})
1	H_2O	18	14	2.3
2	H_2O	18	15	3.5
3	H_2O	100	12	1.1
4	H_2O	100	13	5.0
5	H_2O	100	17	2.3
6	D_2O	18	10	2.3
7	D_2O	18	11	3.5
8	D_2O	18	17	2.3
9	D_2O	30	2.1	3.5
10	D_2O	30	3.2	3.5
11	D_2O	30	8.9	3.5
12	D_2O	30	11	3.5
13	D_2O	40	6	1.7
14	D_2O	40	14	1.1
15	D_2O	40	14	3.5
16	D_2O	60	9.6	1.1
17	D_2O	60	17	3.5
18	D_2O	100	1.5	1.9
19	D_2O	100	2.3	1.8
20	D_2O	100	5.1	2.3
21	D_2O	100	5.3	2.3
22	D_2O	100	6.8	1.8
23	D_2O	100	12	5.0
24	D_2O	100	13	1.1
25	D_2O	100	14	3.5
26	D_2O	100	16	2.3
27	D_2O	100	28	1.7
28	D_2O[a]	30	14	2.3
29	$H_2^{18}O$	20	14	5.0
30	$H_2^{18}O$	30	14	5.0
31	$H_2^{18}O$	100	14	5.0
32	D_2O/H_2O[b]	30	9.5/48	2.3
33	N_2/D_2O[b]	18	20/14	2.3

Notes.
[a]Annealed at 100 K for 1 hr.
[b]Ice layers.

Technology (NIST) calibrated silicon diode and actiometry as described in Öberg et al. (2009).

Table 1 summarizes the experiments in this study. The majority of the photodesorption experiments is carried out with D_2O ice. These experiments are complimented with H_2O and $H_2^{18}O$ experiments to test isotope effects and to ensure the validity of mass spectrometric detections of OH (OD) and H_2O (D_2O) fragments. Layered experiments with H_2O and D_2O at 30 and 100 K and with N_2 on top of D_2O at 18 K are performed to check for substrate effects and to determine the ice-loss behavior when desorption is hindered.

2.2. Data Analysis

The UV-induced ice-loss rate during each H_2O and D_2O experiment is determined by Reflection Absorption Infrared Spectroscopy (RAIRS) of the ice as a function of UV fluence. The intensity of the RAIRS profile is linearly correlated with the ice layer thickness up to ∼20 ML, but the RAIRS profile can be used up to 50 ML for analysis as long as the nonlinear growth above 20 ML is taken into account (Öberg et al. 2009). One ML is generally taken to consist of $\sim 10^{15}$ molecules cm^{-2} and the loss yield, in molecules photon^{-1}, of the original ice is subsequently derived from the intensity loss in the RAIR spectra as a function of fluence.

The determined ice-loss yield is not necessarily the photodesorption yield. H_2O has only dissociative transitions in the wavelength region of the lamp. Hence, the UV irradiation induces photodesorption as well as photochemistry (Gerakines et al. 1996; Westley et al. 1995a). UV irradiation may also induce structural changes in the ice that modify the infrared spectral features. These bulk processes, photolysis and rearrangement, are separated from the photodesorption by exploiting the different kinetic order behavior of bulk processes and surface desorption, i.e., first-order versus zeroth-order processes. This method is described in detail in Öberg et al. (2009).

Using RAIRS to determine the desorption of molecules depends on a reliable conversion between the ice infrared absorbance and the amount of ice molecules. Due to the fact that all ice measurements are done using RAIRS, the ice thickness cannot be estimated from the previously determined ice transmission band strengths. In Öberg et al. (2009), the CO and CO_2-appropriate RAIRS band strengths are reported. The H_2O and D_2O band strengths are estimated by assuming that the relative band strengths of CO, CO_2, and H_2O ices are the same in transmission and reflection–absorption spectra. This is found to be accurate within a factor of 2 by Ioppolo et al. (2008). The thickness uncertainty is then ∼50%. For the conversion between H_2O and CO and CO_2 band strengths, the measured band strengths of Hudgins et al. (1993) are used after modification as suggested by Boogert et al. (1997). The relative band strengths of H_2O and D_2O were measured by Venyaminov & Prendergast (1997). This results in H_2O and D_2O stretching band strengths of 0.95 and 0.68 cm^{-1} ML^{-1}, respectively, for our setup. These band strengths are converted to cm molecule^{-1} assuming an ML density of 10^{15} molecules ML^{-1} cm^{-2}.

Kinetic modeling of the integrated RAIRS profiles as a function of UV fluence and the determined band strengths together provide a total ice photodesorption yield. The simultaneous mass spectrometry of gas-phase molecules during irradiation reveals the nature of the desorbed species, i.e., what proportion of H_2O ice desorbs as H_2O molecules versus photo-produced radicals and molecules. This is limited by the fact that less volatile molecules adsorb onto the heating shield and other semicold surfaces inside the experiment before reaching the mass spectrometer. Hence, the relative abundance of species with very different cryopumping rates, such as H_2 and H_2O, cannot be derived. It is however possible to estimate the ratio of the predicted main desorption species: H_2O and OH.

The main sources of uncertainty in these experiments are the photon flux at the sample surface and ice thickness calibrations of ∼30% and 50%, respectively. In addition, from repeated experiments, the H_2O experimental results vary with 20%. The total uncertainty is hence ∼60% for the total photodesorption rate. The relative desorption yields of different desorption products are more uncertain due to the additional assumptions that go into their derivation, i.e., that the products have similar pumping rates and QMS detection efficiencies. We estimate that the relative desorption yields thus have ∼30% uncertainty in addition to the uncertainty of the total photodesorption yield.

3. RESULTS

3.1. Photodesorption Process and Products

Figure 1 shows the RAIR spectrum of the D_2O stretching band at 40 K as a function of UV fluence. At 40 K the UV photons simultaneously induce dissociation of bulk D_2O ice and desorption of surface molecules. This is clearly seen in

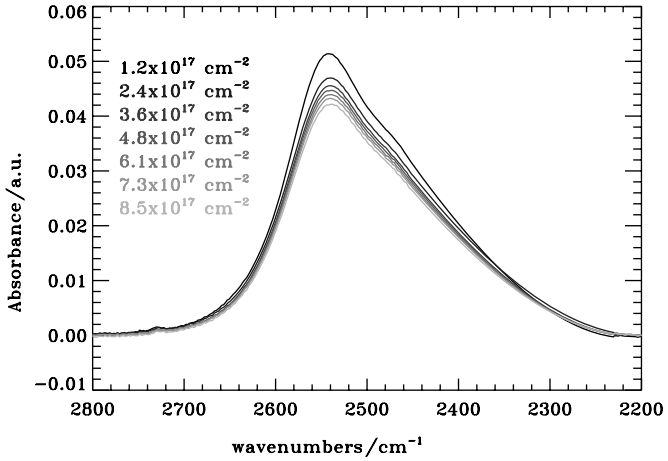

Figure 1. Spectra of the D_2O stretching mode at 40 K as a function of UV fluence. The decreasing ice-loss yield with fluence is due to the fact that ice is lost through a combination of bulk photolysis and photodesorption. The small bump at 2730 cm^{-1} is probably caused by the free OD stretch.

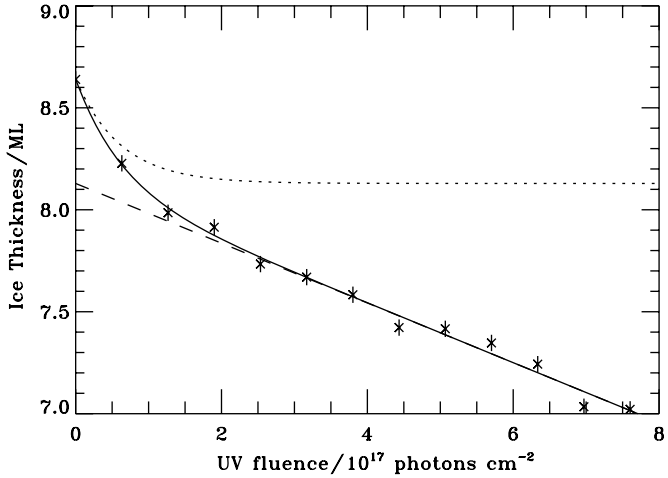

Figure 2. D_2O ice layer thickness as a function of UV fluence together with the fit (solid line), which is split up in ice loss due to bulk photolysis (dotted line) and photodesorption (dashed line). The fitted bulk photolysis contribution is offset for visibility.

Figure 2, where the ice thickness is plotted versus UV fluence. The ice loss is modeled by a combination of an exponential function and a linear function, where the exponential function describes the photolysis of bulk D_2O as a first-order process similarly to Cottin et al. (2003). The linear part of the ice loss is interpreted as photodesorption of surface molecules, which should be a zeroth-order process (Öberg et al. 2007b). To test that this model holds, a D_2O ice is irradiated at 18 K when covered by a thick N_2 ice, which hinders desorption. The ice-loss curve is then very well fitted ($\chi^2 = 1.8$ for 13 data points) by the exponential function derived from a bare 18 K ice. This shows that the observed exponential decay is indeed due to bulk photolysis with a possible contribution from ice rearrangement. As discussed below the ice structure is affected by the UV irradiation, but this rearrangement seems complete within an UV fluence of 1×10^{17} photons cm^{-2}. It may hence contribute somewhat to the exponential decay of the RAIRS profile, but is completely filtered out from the photodesorption rate determination.

There are no other species than H_2O (D_2O) visible in the RAIR spectra at any temperature. OH (OD) formation cannot be excluded, however, due to the spectral overlap of OH (OD) and

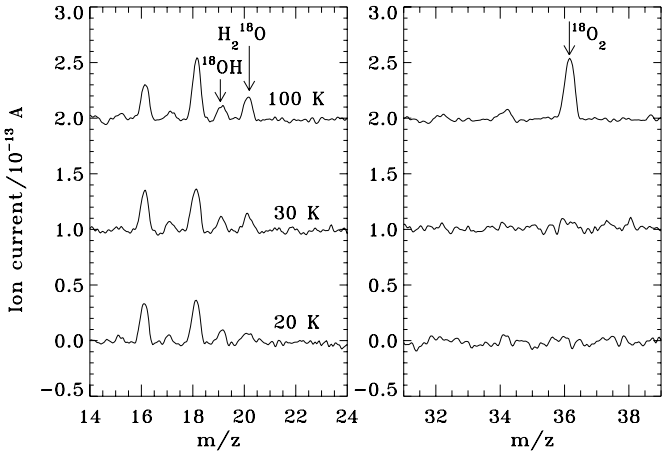

Figure 3. Mass spectra recorded during irradiation of a 14 ML thick $H_2^{18}O$ ice at 20, 30, and 100 K. In addition to photodesorbed ice product signals, background signals from H_2O, OH, O, and O_2 are also seen.

H_2O (D_2O) transitions. Despite this overlap, photolysis of H_2O into OH will result in a measured decrease of the H_2O stretching band area. This is both because of the expected lower band strength of OH compared to H_2O and because the remaining H_2O stretching band strength decreases when the H_2O network is disturbed by other molecules or fragments (Öberg et al. 2007a; Bouwman et al. 2007). The lack of H_2O_2 formation is in contrast to, e.g., Gerakines et al. (1996). This is not a contradictory result however, since less than 0.1% of the H_2O ice is expected to be converted after a similar fluence, which is close to the detection limit here for the strongest H_2O_2 band at 2850 cm^{-1} (Giguère & Harvey 1959).

During irradiation H_2 (D_2) is always detected by the mass spectrometer. At the highest fluxes OH (OD) and H_2O (D_2O) are detected as well. A 14 ML $H_2^{18}O$ ice is irradiated at 20, 30 and 100 K while acquiring mass spectra (Figure 3) to quantify the relative desorption amounts of OH and H_2O without any overlap with background H_2O. The figure shows that the desorbing fraction of OH and H_2O changes somewhat with temperature from 1.0:0.7 at 20 K to 1.2:1.4 at 30 K to 1.2:2.0 at 100 K. No other species are observed at 20 and 30 K. In contrast, at 100 K, O_2 is photodesorbed as well. It is important to note that O_2 and H_2O have very different cryopumping rates and hence their relative mass spectrometric signals are not representative of their relative desorption rates. The upper limit of O_2 desorption is estimated from the fact that a factor of 1.9 more OH and H_2O is detected at 100 K compared to at 20 K, while the total photodesorption rate from RAIRS increases by a factor of 2.4. Hence, at most one fifth of the H_2O photodesorbs as O_2 at high temperatures. Desorption of H_2O_2 cannot be excluded, even though it is not detected, since it is notoriously difficult to detect with a QMS. No buildup of H_2O_2 is observed in the ice, which makes it unlikely that a large part of the ice is desorbed in the form of H_2O_2. Disregarding the small amount of H_2O that does not desorb as either OH or H_2O, the H_2O yield relative to the total photodesorption yield is fitted linearly as a function of temperature for the 14 ML thick ice. This empirical fit yields an expression for the H_2O yield, Y_{pd,H_2O}, as a function of the total photodesorption yield, Y_{pd}:

$$Y_{pd,H_2O} = f_{H_2O} \times Y_{pd}, \quad (1)$$

$$f_{H_2O} = (0.42 \pm 0.07) + (0.002 \pm 0.001) \times T, \quad (2)$$

$$f_{H_2O} + f_{OH} \sim 1, \quad (3)$$

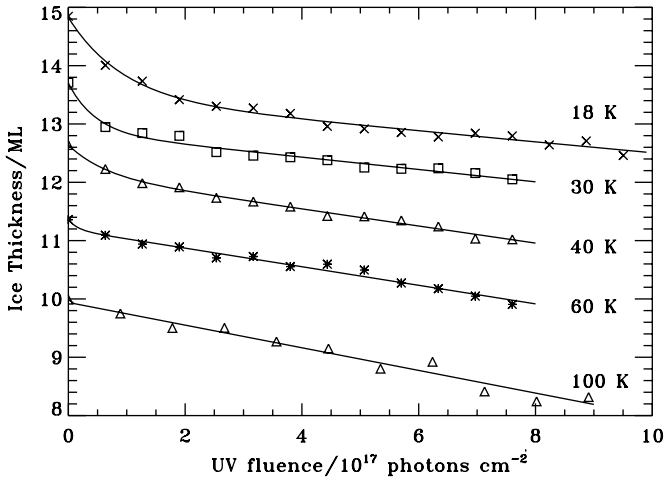

Figure 4. Ice thickness (in ML) vs. photon fluence (in 10^{17} photons cm^{-2}) for ~10 ML D_2O ices at different temperatures, displaying the temperature-dependent degree of ice bulk photolysis vs. ice photodesorption. The curves are offset for visibility. At lower temperatures, the bulk photolysis dominates the ice loss, while it is not visible above 60 K. Simultaneously the photodesorption rate, the slope of the linear part of the ice loss, increases with temperature.

where f_x is the fraction of the total photodesorption that occurs through species x. The relative yields are probably somewhat thickness dependent (Andersson et al. 2006), but due to experimental constraints it is not possible to probe the relative yields for thinner ices.

3.2. Yield Dependences on Temperature, Fluence, Ice Thickness, Flux, and Isotope

3.2.1. Temperature and Photon Fluence

Figure 4 shows the combined bulk photolysis and photodesorption for ~10 ML thick D_2O ices between 18 and 100 K. The ice loss is dominated by bulk photolysis at low temperatures and by photodesorption at higher temperatures. This conclusion follows from the observed facts that (1) the degree of steady-state photolysis decreases with temperature and (2) that the photodesorption yield per incident photon, as measured by the slope of the linear part of the fit, increases with temperature. This increase in photodesorption yield with temperature is shown explicitly in Figure 5(a). Between 18 and 100 K the dependence of the photodesorption yield on temperature for thick ices (greater than 8 ML) is empirically fitted with a linear function

$$Y_{\rm pd}(T, x > 8) = 10^{-3}\,(1.3\,(\pm 0.4) + 0.032\,(\pm 0.008) \times T)\,, \quad (4)$$

where T is the temperature in K and x the ice thickness in ML. The uncertainties are the model fit errors—the total uncertainty of the yield is 60% as stated above.

Figure 4 also shows that the onset of photodesorption is immediate, i.e., there is no fluence dependence, which is opposite to what was observed by Westley et al. (1995a). This difference may be explained by a nonlinear H_2O freezeout during the experiment, which is observed in this experiment (Figure 6) and probably present in the Westley experiment as well. Even under UHV conditions there is always some H_2O present in the vacuum chamber. In our experiment, this leads to an ice deposition rate of ~0.1 ML hr^{-1} at equilibrium, but up to 1 ML hr^{-1} is deposited during the first hour after cool down, which is of the same order as the photodesorption rate presented in Westley et al. (1995a). In their setup, it would not have been possible to separate this increased freezeout rate from a lower desorption rate at the beginning of each experiment. This problem is circumvented here by using D_2O for most experiments and by letting the H_2O freezeout reach equilibrium before starting the experiment.

3.2.2. Substrate and Ice Structure Effects

In Figure 5(a), one of the two additional points at 30 K represents the yield from a 9.5 ML D_2O ice deposited on top of a H_2O ice layer, showing that the substrate has no effect on the desorption yield. At 100 K, this cannot be investigated due to mixing of the two layered ices, but D_2O experiments with different ice thicknesses indicate that the substrate has no effect at any temperature for ices thicker than 2 ML (Figure 5(b)).

The structure independence seen by Westley et al. (1995a) is also confirmed here for a 30 K ice that is annealed at 100 K, until the spectra display a low-frequency shoulder typical for crystalline ice (Hagen 1981), and is subsequently cooled down (the second additional point at 30 K in Figure 5(a)). Figure 7 shows that this can be explained by the fact that the annealed ice returns to an amorphous state upon irradiation with less than 10^{16} UV photons. At 100 K the irradiation does not yield amorphous ice, probably because the temperature is high enough for displaced molecules to diffuse back into a crystalline structure.

3.2.3. Ice Thickness

At 100 K, where photodesorption completely dominates over bulk photolysis, there is no photodesorption yield dependence on ice thickness for D_2O ices between 8 and 28 ML (Figure 5(b)) suggesting that the H_2O ice photodesorption is only important in the top few layers. At 30 K the photodesorption yield is constant down to at least 3 ML. At both temperatures, the thickness dependence is fitted by a function of the type

$$Y(T, x) = Y_{\rm pd}(T, x > 8)(1 - e^{-x/l(T)}), \quad (5)$$

where $Y(T, x)$ is the thickness and temperature-dependent photodesorption yield, $Y_{\rm pd}(T, x > 8)$ is the yield for thick ices at a certain temperature, x is the ice thickness and $l(T)$ is an ice diffusion parameter, whose origin is discussed further below. The IDL routine $mpfit$ is used to fit the data with the results: $l(100\ {\rm K}) = 3.0 \pm 1.0$ ML and $l(30\ {\rm K}) < 2.7$ ML, with the best fit of $l(30\ {\rm K}) = 1.3$ ML shown in Figure 5(b). Thus, photodesorption occurs deeper in the ice at 100 K compared to at 30 K by at least a factor of 2. Extrapolating this to lower temperatures gives

$$l(T) \sim 0.6 + 0.024 \times T. \quad (6)$$

3.2.4. Lamp Flux

The independence of the photodesorption yield on lamp flux found by Westley et al. (1995a) for higher fluxes ($1–5 \times 10^{14}$ photons cm^{-2} s^{-1}) is also seen in this study between 1.1 and 5.0×10^{13} photons cm^{-2} s^{-1} for different temperatures and is shown for 100 K ices in Figure 5(c).

3.2.5. H_2O Versus D_2O

Within the experimental uncertainties, there is no difference between the H_2O and D_2O photodesorption yields at 18 or 100 K (Figure 5(d)). It should be noted that at 18 K the photodesorption yield of H_2O is highly uncertain, because the H_2O freezeout rate dominates over the photodesorption rate during the experiment. Nevertheless, these experiments support the direct applicability of above results, on D_2O ices, to H_2O ices.

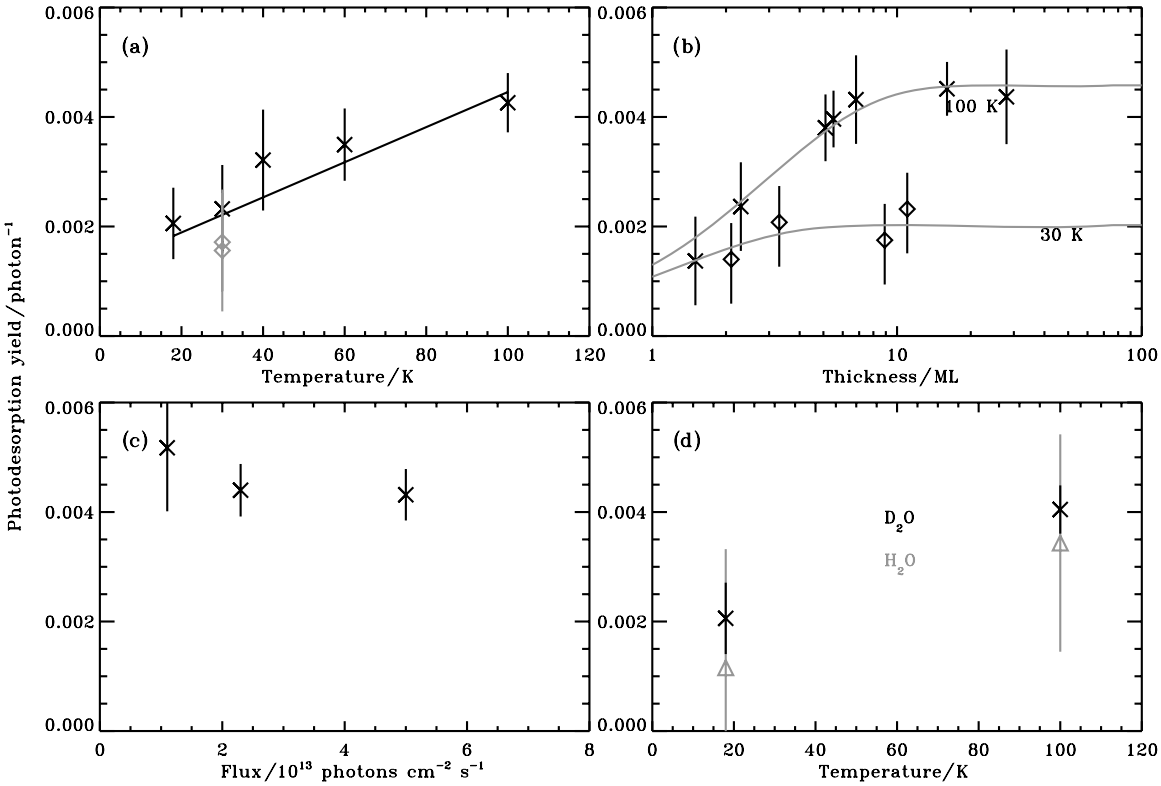

Figure 5. D_2O photodesorption yield as a function of temperature (a), ice thickness (b), lamp flux (c), and isotope (d). In the temperature plot (a) the ices are ∼10 ML thick. The two gray diamonds mark the desorption rate from a D_2O:H_2O layered ice and an annealed ice. In panel (b), the thickness dependence is plotted and fitted for ices at 30 and 100 K. In panel (c), the ices are 12–16 ML thick and irradiated at 100 K. The experiments marked with gray triangles in panel (d) are carried out with H_2O instead of D_2O.

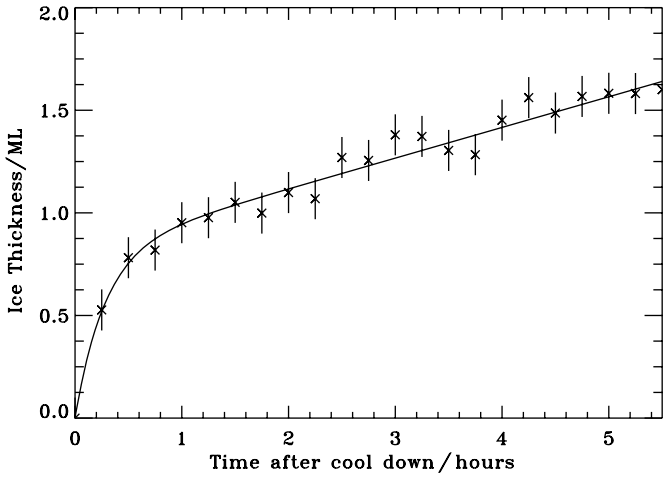

Figure 6. Buildup of H_2O following cool down to 18 K (without UV irradiation), which is due to the small H_2O contamination always present, also under UHV conditions. The nonlinear behavior is a result of the time required to reach steady state between H_2O freezeout on the substrate, the desorption of adsorbed H_2O from the chamber walls, and the H_2O pumping.

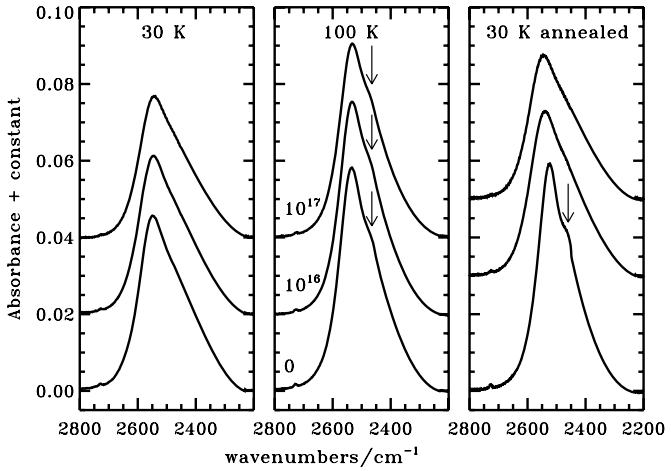

Figure 7. Spectra of ices at 30 K (left) and 100 K (middle), and at 30 K, but deposited at 100 K (right), before onset of irradiation and after irradiation by ∼10^{16} and 10^{17} photons cm^{-2} as indicated in the middle figure. Note the disappearance of the crystalline feature around 2460 cm^{-1} (marked with the arrows) with increasing UV fluence for the annealed ice.

4. DISCUSSION

4.1. H_2O Photodesorption Mechanism

The UV photodesorption mechanism of H_2O ice does not depend on flux or substrate and is hence most likely due to direct absorption of UV light by H_2O molecules, resulting in dissociation of the molecule into fragments with excess energy. The experiments show that once dissociated one of the four different outcomes ensues: the dissociated fragments (1) photodesorb directly, (2) recombine and photodesorb or kick out a surface H_2O molecule, (3) freeze out in the ice, or (4) recombine and freeze out in the ice. These are the same outcomes described in Andersson et al. (2006) when performing molecular dynamic simulations on H_2O photodesorption. At high temperatures (100 K) the dissociated OH or O fragments are also mobile enough to recombine to, e.g., O_2.

The importance of the different pathways depends both on the temperature and where in the ice the molecule is dissociated.

With increasing temperature the mobility of molecules, atoms, and radicals is expected to increase. This, among other things, increases the reaction probability of OH and H. Assuming the same dissociation yield at all temperatures, the amount of radicals in the ice should then decrease with temperature since the increased mobility with temperature increases the recombination rate. This agrees well with the observed decrease in the steady-state photolysis yield between 18 and 100 K (Figure 4). The increased recombination rate also explains the increasing H_2O/OH gas-phase ratio with temperature during photodesorption. Finally, the increased mobility of OH may also account for the observed photodesorbed O_2 at 100 K and its absence at temperatures below 30 K. Although it cannot be excluded that the O_2 forms also at lower temperatures and is thermally desorbed following formation above 30 K (Acharyya et al. 2007).

The increased mobility with temperature is also reflected in the ice thickness experiments, where the photodesorption occurs down to greater depths in the ice at 100 K compared to 30 K. The factor of 2 or larger penetration depth into the ice at 100 K compared to 30 K (Figure 5(b)) agrees well with the increase of the photodesorption yield between 30 and 100 K (Figure 5(a)). The increased photodesorption yield with temperature is then most likely due to an increased mobility rather than the overcoming of reaction barriers, as suggested by Westley et al. (1995b).

The simulations of Andersson et al. (2006) for an ice at 10 K indicate that photodesorption is only efficient in the top two to three layers for cold ices. At larger depths freezeout of the dissociation products completely dominates. This is in excellent agreement with the results of the thickness-dependent experiments at 30 K, where photodesorption is only important in the top three ML. The simulation is run at ps timescales, while the experiments cover several hours. The agreement for low temperatures between theory and experiment hence indicates that only short timescale processes matter for determining the photodesorption yield at temperatures below 30 K. At higher temperatures longer timescale processes, such as thermal diffusion and desorption, increase in importance.

As mentioned above, the depth at which photodesorption occurs increases with temperature, but still there is a certain ice depth where freezeout of the recombined H_2O is the only outcome. At 100 K the measurements are accurate enough to confirm that the mobility of the molecules following photodissociation and recombination is well described by a mean-free-path type model $c \times (1 - e^{-x/l(T)})$, where x is the ice thickness, l is the diffusion mean free path, and c is the maximum desorption yield for infinitely thick ice. This is also the case for CO_2 photodesorption fragments (Öberg et al. 2009) and may hence be a universal feature for molecules that photodesorb following dissociation. This mean-free-path behavior is best explained with the desorption of the energetic photodissociation product or recombined molecule itself, but does not exclude the other outcome of the molecular simulations, i.e., that H_2O molecules also desorb indirectly from a kick of a H atom, which originates from the photodissociation of another H_2O molecule.

4.2. Comparison with Previous Experiments

The results here agree on several important points with those of Westley et al. (1995a, 1995b). The maximum total photodesorption yields (H_2O + OH) are the same within the reported uncertainties of both experiments. The determined photodesorption yield is likely a robust value, which is not significantly affected by different lamp spectral energy distributions (SEDs), order of magnitude different UV fluxes and ice thicknesses. The present study also agrees with Westley et al. (1995a, 1995b) on the photodesorption yield dependence on temperature and on the identification of the main desorption products—H_2, O_2 and H_2O—with the one exception that we also detect OH.

The apparent fluence dependence in the Westley experiment can be explained with H_2O freezeout during the early stages of the experiment, especially since they mention a large H_2O background pressure in their experiment. This is also in agreement with the mass spectrometer measurements of desorbed species shown in their paper (H_2 and O_2), which do not show any fluence-dependent yields. The apparent fluence dependence led Westley et al. (1995a) to suggest that at low temperatures desorption occurs through reactions between O and OH. They subsequently claimed that while low-temperature photodesorption occurs through photochemistry, high-temperature photodesorption is a direct process. From the experiments here, it is more likely that both low- and high-temperature photodesorption processes are dominated by direct photodesorption, but at high temperatures there is some additional desorption due to photochemistry of OH and O fragments.

Ion sputtering of ices has been more thoroughly investigated than ice photodesorption and recent experiments by Famá et al. (2008) on the temperature dependence of ion sputtering of H_2O ice suggest that the desorption mechanism is comparable for photodesorption and ion sputtering following the initial excitation by a photon or an ion. In particular, in both photodesorption and ion sputtering experiments, the desorption seems highly dependent on the formation and subsequent behavior of radicals and molecular products in the ice. More results are however required on, e.g., the thickness dependence and the resulting desorption products during ion sputtering to make an actual comparison between the two processes. The absolute ion-sputtering yield of H_2O depends on both the ion energy and ionic species, but it is generally a factor of 10^3–10^4 higher than photodesorption yields, i.e., close to unity. When evaluating the importance of the two processes in an astrophysical setting, it is important to note that the ion flux in most regions is orders of magnitude lower than the UV flux.

4.3. Astrophysical Consequences

This study shows that pure H_2O ice photodesorbs directly or indirectly following fast intermediate photochemistry during which the photodissociated fragments recombine. The mechanism hence does not depend on the photon flux level or on buildup of radicals in the ice. This means that the yield derived in the laboratory can be directly applied to astrophysical environments. Deep into clouds and disks the rate may be considerably reduced due to, e.g., CO ice covers. At the edges of clouds and disks, where other ices have not yet formed at large abundances, the rate for pure H_2O ice is directly applicable. Here, as a test case, it is applied to the disk surrounding a Herbig Ae/Be star using models developed by Dullemond et al. (2001) and Dullemond & Dominik (2004) to fit the observed SEDs of these objects. In the model, the physical disk model is static and the chemistry is kept very simple, only including H_2O freezeout, thermal and nonthermal desorption, and no gas-phase chemical network except for the recombination of OH to form H_2O.

The model star has a mass of 2.5 $M_\odot$, a radius of 2.0 $R_\odot$, and an effective temperature of 10,500 K, typical of a Herbig Ae/Be star, and it emits a pure blackbody spectrum. The accompanying

disk has a mass of 0.01 $M_\odot$, with an R^{-1} surface density profile, and an outer radius of 300 AU. To avoid a sharp truncation, the surface density decreases as R^{-12} beyond the outer radius. The inner radius is set by a dust evaporation temperature of 1700 K. The radiation field and dust temperature throughout the disk are calculated using the radiative transfer package RADMC (Dullemond & Dominik 2004) and the resulting disk is in vertical hydrostatic equilibrium, with a flaring shape. The gas temperature is set equal to the dust temperature.

Gas-phase H_2O is initially distributed uniformly throughout the disk at a constant abundance of $1.8 \times 10^{-4} \times n_H$, where n_H is the total number of hydrogen nuclei. This is somewhat artificial since H_2O forms on grain surfaces, but if the model is run long enough (here to $\sim 10^6$ years) the final distribution will not depend on the initial distribution between the gas and the grain. The H_2O freezes out or adsorbs onto grain surfaces with the rate coefficient k_{ads},

$$k_{ads} = (4.55 \times 10^{-18}\ \mathrm{cm^3\ K^{-1/2} s^{-1}}) n_H \sqrt{\frac{T_g}{M}}, \quad (7)$$

where T_g is the gas temperature and M is the molecular weight of water. The numerical factor assumes unit sticking efficiency, a mean grain radius of 0.1 μm and a grain abundance of 10^{-12} with respect to H_2 (Charnley et al. 2001). Once adsorbed onto the grains, the H_2O desorbs thermally with a rate coefficient k_{thd},

$$k_{thd} = (1.26 \times 10^{-21}\ \mathrm{cm^2}) A \frac{n_H}{n_s} e^{-\frac{E_b}{kT_{gr}}}, \quad (8)$$

where n_s is the number density of solid water and T_{gr} is the grain temperature. The numerical factor assumes the same grain properties as in Equation (7) and 10^6 binding sites per grain. The pre-exponential factor, A, and the binding energy, E_b/k, are set to 1×10^{30} cm^{-2} s^{-1} and 5773 K, respectively (Fraser et al. 2001). Finally, the H_2O photodesorption rate coefficient k_{pd} is defined as

$$k_{pd} = (3.14 \times 10^{-14} \mathrm{s^{-1}}) G_0 n_H Y_{pd}, \quad (9)$$

where the numerical factor describes the UV photon flux onto a grain surface per unit time for the average interstellar field (10^8 photons cm^{-2} s^{-1}), G_0 is the scaling factor for the UV field that is output by RADMC for each grid point, and Y_{pd} is the photodesorption yield. In addition to the external UV field a cosmic-ray-induced field is approximated by setting a lower limit on G_0 of 10^{-4} (Shen et al. 2004). The photodesorption results in the release of both OH and H_2O. The released OH is quickly rehydrogenated in the model in the gas, however, and hence we let all H_2O ices desorb as H_2O molecules with the yield,

$$Y_{pd,H_2O}(T_{gr}, x) = 10^{-3}(1.3 + 0.032 \times T_{gr})(1 - e^{-x/l(T)}), \quad (10)$$

where x is the ice thickness in ML and $l(T)$ is the temperature-dependent diffusion length in ML (Equation (6)). The model is run for two scenarios: (1) without and (2) with photodesorption. Each run is 3 Myr, the typical age of a Herbig disk, which results in steady-state gas- and grain-phase abundances. Figure 8(a) shows the gas-phase H_2O fraction in the disk without photodesorption as a function of radial and vertical distances from the central protostar. As expected the H_2O is completely frozen out, except in the surface layer, when nonthermal

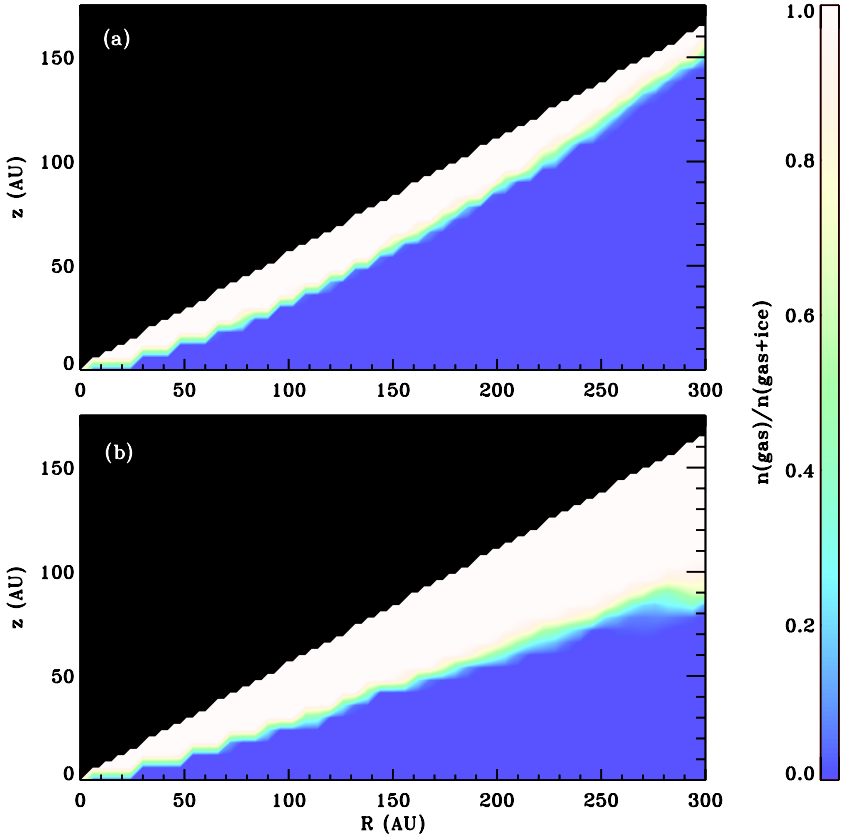

Figure 8. Simulation of the distribution of gas phase over total H_2O ratio in a circumstellar disk without (a) and with (b) photodesorption. The white, H_2O-gas-dominated area extends more than 50 AU deeper into the disk when photodesorption is included, illustrating the large impact of photodesorption on the chemistry in the outer parts of disks.

desorption is excluded (Figure 8(a)). When photodesorption is turned on, H_2O is kept in the gas phase further in toward the midplane (Figure 8(b)). Without photodesorption, 0.6% of the H_2O in the disk is in the gas phase at temperatures above the thermal desorption temperature of 100 K and 0.002% is in the gas phase below 100 K. With photodesorption included in the model, 0.6% of the H_2O is still present as warm gas, but now 2% of the total H_2O is in the gas phase at temperatures below 100 K. The total column density of warm $T > 100$ K H_2O gas, averaged over the entire disk, is hence the same in both cases (1.4×10^{17} cm^{-2}). In contrast, the amount of cold H_2O gas averaged over the entire disk increases from 5.0×10^{14} to 4.5×10^{17} cm^{-2} when photodesorption is turned on. This means that a gas-phase chemistry involving OH or H_2O is possible deep toward the disk midplane also in the outer disk. For comparison we also run our model using a constant surface photodesorption yield of 10^{-3}, which has often been used in the literature previously. For this particular model the total column density changes with less than a factor of 2 compared to using the derived yield equation from this study. The spatial distribution of gas-phase H_2O is however different using the different yields due to the fact that using the constant yield overestimates the desorption rate in the surface region and underestimates it deeper into the disk.

This is a generic disk model commonly used to model disks around intermediate-mass stars. To model an actually observed object would require a more detailed model that takes into account observed constraints on the disk structure. In addition, the calculated gas-phase abundances may change somewhat when chemistry is taken into account. The general trend is however that photodesorption increases the amount of cold gas-phase H_2O by orders of magnitude. This is also the result of a recent photodissociation region (PDR) model showing that the inclusion of chemistry, while important for more accurate predictions, will not reduce the predicted column density of gas-phase H_2O dramatically (Hollenbach et al. 2009). Other effects such as grain growth may increase the photodesorption rate, but without a full chemical network it is unclear how much of this increase will be off-set by photodissociation of the desorbed H_2O. Probably only observations of cold H_2O on the scale of protoplanetary disks will yield an answer. The beam of the imminent *Herschel Space Observatory* is of the same order of magnitude as this modeled disk and hence these results show that large amounts of cold H_2O will be observable. For exactly this purpose—to observe cold H_2O gas—the WISH program was approved as a *Herschel* key program. The amount of gas-phase H_2O in disks due to nonthermal desorption may hence be answered very soon indeed.

5. CONCLUSIONS

1. The total D_2O and H_2O photodesorption yields are indistinguishable within the experimental uncertainties and are empirically described by $Y_{\rm pd}(T, x) = Y_{\rm pd}(T, x > 8)(1 - e^{-x/l(T)})$ where $Y_{\rm pd}(T, x)$ is the thickness and temperature-dependent photodesorption yield, x is the ice thickness in MLs, and $l(T)$ is an ice diffusion parameter that varies between 1.3 ML at 30 K and 3.0 ML at 100 K.
2. For thick ices (greater than 8 ML), the yield depends linearly on temperature such that $Y_{\rm pd}(T, x > 8) = 10^{-3}\,(1.3 + 0.032 \times T)$ photon^{-1}. The yields agrees, within the reported 60% uncertainty, with a previous experiment (Westley et al. 1995a).
3. The nature of the desorbed species is temperature dependent, with equal amounts of OH and H_2O detected at low temperatures. At higher temperatures the H_2O:OH fraction is ~2:1 and in addition about a fifth of the ice photodesorbs as heavier fragments like O_2. The fraction of the total photodesorption yield that results in H_2O molecules desorbing is described by $f_{\rm H_2O} = (0.42 \pm 0.07) + (0.002 \pm 0.001) \times T$.
4. We find no yield dependence on photon flux or fluence. The fluence independence is in contrast with a previous experiment (Westley et al. 1995a).
5. We also find no dependence on the ice structure, i.e., whether the D_2O ice is amorphous or crystalline. This is consistent with spectroscopic evidence of fast destruction of crystalline ice into an amorphous state following UV irradiation.
6. The photodesorption yield and dependences found here are consistent with previous theoretical predictions of H_2O photodesorption, where the photodesorption is limited to the top few layers of the ice (Andersson et al. 2006). In addition, we see that the photodesorption yield increases with ice temperature because of the increased mobility of the photolysis fragments, allowing desorption from deeper within the ice.
7. Applying the experimental yield to a Herbig Ae/Be star+disk model we calculate that the predicted amount of cold (less than 100 K) gas-phase H_2O, averaged over the entire disk, increases with orders of magnitude due to photodesorption.

The authors thank Stefan Andersson and Herma Cuppen for stimulating discussions. Funding is provided by NOVA, the Netherlands Research School for Astronomy, a grant from the European Early Stage Training Network ("EARA" MEST-CT-2004-504604), and a Netherlands Organization for Scientific Research (NWO) Spinoza grant.

REFERENCES

Acharyya, K., Fuchs, G. W., Fraser, H. J., van Dishoeck, E. F., & Linnartz, H. 2007, A&A, 466, 1005
Allamandola, L. J., Sandford, S. A., & Valero, G. J. 1988, Icarus, 76, 225
Andersson, S., Al Halabi, A., Kroes, G.-J., & van Dishoeck, E. F. 2006, J. Chem. Phys., 124, 4715
Andersson, S., & van Dishoeck, E. F. 2008, A&A, 491, 907
Bergin, E. A., Langer, W. D., & Goldsmith, P. F. 1995, ApJ, 441, 222
Boogert, A. C. A., & Ehrenfreund, P. 2004, in ASP Conf. Ser. 309, Astrophysics of Dust, ed. A. N. Witt, G. C. Clayton, & B. T. Draine (San Francisco, CA: ASP), 547
Boogert, A. C. A., Schutte, W. A., Helmich, F. P., Tielens, A. G. G. M., & Wooden, D. H. 1997, A&A, 317, 929
Boonman, A. M. S., & van Dishoeck, E. F. 2003, A&A, 403, 1003
Bouwman, J., et al. 2007, A&A, 476, 995
Brown, W. L., Lanzerotti, L. J., Poate, J. M., & Augustyniak, W. M. 1978, Phys. Rev. Lett., 40, 1027
Ceccarelli, C., et al. 1999, A&A, 342, L21
Cernicharo, J., et al. 1990, A&A, 231, L15
Charnley, S. B. 1997, ApJ, 481, 396
Charnley, S. B., Rodgers, S. D., & Ehrenfreund, P. 2001, A&A, 378, 1024
Charnley, S. B., Tielens, A. G. G. M., & Millar, T. J. 1992, ApJ, 399, L71
Cottin, H., Moore, M. H., & Bénilan, Y. 2003, ApJ, 590, 874
d'Hendecourt, L. B., Allamandola, L. J., Baas, F., & Greenberg, J. M. 1982, A&A, 109, L12
Dominik, C., Ceccarelli, C., Hollenbach, D., & Kaufman, M. 2005, ApJL, 635, L85
Dullemond, C. P., & Dominik, C. 2004, A&A, 417, 159
Dullemond, C. P., Dominik, C., & Natta, A. 2001, ApJ, 560, 957
Elitzur, M., & de Jong, T. 1978, A&A, 67, 323
Elitzur, M., & Watson, W. D. 1978, ApJ, 222, L141

Famá, M., Shi, J., & Baragiola, R. A. 2008, Surf. Sci., 602, 156
Franklin, J., et al. 2008, ApJ, 674, 1015
Fraser, H. J., Collings, M. P., McCoustra, M. R. S., & Williams, D. A. 2001, MNRAS, 327, 1165
Fuchs, G. W., et al. 2006, Faraday Discuss., 133, 331
Gensheimer, P. D., Mauersberger, R., & Wilson, T. L. 1996, A&A, 314, 281
Gerakines, P. A., Schutte, W. A., & Ehrenfreund, P. 1996, A&A, 312, 289
Giguère, P. A., & Harvey, K. B. 1959, J. Mol. Spectrosc., 3, 36
Hagen, W. 1981, Chem. Phys., 56, 367
Hjalmarson, Å., et al. 2003, A&A, 402, L39
Hollenbach, D., Kaufman, M. J., Bergin, E. A., & Melnick, G. J. 2009, ApJ, 690, 1497
Hudgins, D. M., Sandford, S. A., Allamandola, L. J., & Tielens, A. G. G. M. 1993, ApJS, 86, 713
Ioppolo, S., Cuppen, H. M., Romanzin, C., van Dishoeck, E. F., & Linnartz, H. 2008, ApJ, 686, 1474
Jacq, T., Henkel, C., Walmsley, C. M., Jewell, P. R., & Baudry, A. 1988, A&A, 199, L5
Knacke, R. F., & Larson, H. P. 1991, ApJ, 367, 162
Léger, A., Jura, M., & Omont, A. 1985, A&A, 144, 147
Melnick, G. J., & Bergin, E. A. 2005, Adv. Space Res., 36, 1027
Melnick, G. J., et al. 2000, ApJ, 539, L87
Miyauchi, N., et al. 2008, Chem. Phys. Lett., 456, 27
Muñoz Caro, G. M., & Schutte, W. A. 2003, A&A, 412, 121
Nisini, B., et al. 1999, A&A, 350, 529
Öberg, K. I., van Dishoeck, E. F., & Linnartz, H. 2009, A&A, in press
Öberg, K. I., et al. 2007a, A&A, 462, 1187
Öberg, K. I., et al. 2007b, ApJ, 662, L23
Shen, C. J., Greenberg, J. M., Schutte, W. A., & van Dishoeck, E. F. 2004, A&A, 415, 203
Snell, R. L., et al. 2000, ApJ, 539, L101
Tielens, A. G. G. M., & Hagen, W. 1982, A&A, 114, 245
van der Tak, F. F. S., Walmsley, C. M., Herpin, F., & Ceccarelli, C. 2006, A&A, 447, 1011
van Dishoeck, E. F. 2006, PNAS, 103, 12249
van Dishoeck, E. F., Blake, G. A., Draine, B. T., & Lunine, J. I. 1993, in Protostars and Planets III, ed. E. H. Levy & J. I. Lunine (Tuscon, AZ: Univ. of Arizona), 163
van Dishoeck, E. F., & Helmich, F. P. 1996, A&A, 315, L177
van Kempen, T. A., Doty, S. D., van Dishoeck, E. F., Hogerheijde, M. R., & Jørgensen, J. K. 2008, A&A, 487, 975
Venyaminov, S., & Prendergast, F. 1997, Anal. Biochem., 248, 234
Watanabe, N., Horii, T., & Kouchi, A. 2000, ApJ, 541, 772
Westley, M. S., Baragiola, R. A., Johnson, R. E., & Baratta, G. A. 1995a, Nature, 373, 405
Westley, M. S., Baragiola, R. A., Johnson, R. E., & Baratta, G. A. 1995b, Planet. Space Sci., 43, 1311
Willacy, K. 2007, ApJ, 660, 441
Willacy, K., & Langer, W. D. 2000, ApJ, 544, 903
Wilson, C. D., et al. 2003, A&A, 402, L59
Yabushita, A., Kanda, D., Kawanaka, N., Kawasaki, M., & Ashfold, M. N. R. 2006, J. Chem. Phys., 125, 3406